

Mass Estimation of Merging Galaxy Clusters

Motokazu TAKIZAWA¹ Ryo NAGINO² and Kyoko MATSUSHITA²

¹*Department of Physics, Yamagata University, 1-4-12 Kojirakawa-machi, Yamagata 990-8560*

takizawa@sci.kj.yamagata-u.ac.jp

²*Department of Physics, Tokyo University of Science, 1-3 Kagurazaka, Shinjuku-ku, Tokyo 162-8601*

(Received 0 0; accepted 0 0)

Abstract

We investigate the impact of mergers on the mass estimation of galaxy clusters using N -body + hydrodynamical simulation data. We estimate virial mass from these data and compare it with real mass. When the smaller subcluster's mass is larger than a quarter of that of the larger one, virial mass can be larger than twice of the real mass. The results strongly depend on the observational directions, because of anisotropic velocity distribution of the member galaxies. We also make the X-ray surface brightness and spectroscopic-like temperature maps from the simulation data. The mass profile is estimated from these data on the assumption of hydrostatic equilibrium. In general, mass estimation with X-ray data gives us better results than virial mass estimation. The dependence upon observational directions is weaker than in case of virial mass estimation. When the system is observed along the collision axis, the projected mass tends to be underestimated. This fact should be noted especially when the virial and/or X-ray mass are compared with gravitational lensing results.

Key words: galaxies: clusters: general — hydrodynamics — cosmology: dark matter — X-rays: galaxies: clusters

1. Introduction

Mass is one of the most important physical parameters to characterize astrophysical objects. This is especially true in many kinds of self-gravitating objects such as star clusters, galaxies, and clusters of galaxies, where gravity plays a crucial role in their evolution. In addition, mass distribution in large scales in the universe have some information about dark matter (DM). For example, mass distribution in the very central part of relaxed dark halos could be altered by the self-interaction of DM particles (Yoshida et al. 2000). Investigating spatial distributions of DM, galaxies, and intracluster medium (ICM) also gives us important clues of DM properties (Clowe et al. 2004; Bradač et al. 2006; Jee et al. 2007; Okabe & Umetsu 2008).

There are several methods to estimate mass distribution of galaxy clusters in an observational way. Assuming dynamical equilibrium, we can estimate cluster mass from line-of-sight velocity distribution of member galaxies through virial theorem or Jeans equation (Kent & Gunn 1982; Oegerle & Hill 1994; Girardi et al. 1998; Barrena et al. 2007; Maurogordato et al. 2008). Cluster mass distribution can also be estimated from the X-ray observational data on the assumption of hydrostatic equilibrium of the ICM (Reiprich & Böhringer 2002; Takizawa et al. 2003; Ota et al. 2004; Vikhlinin et al. 2006; Gastaldello et al. 2007). Weak and strong gravitational lensing techniques enable us to determine gravitational mass directly without any assumptions of dynamical status of the system (Kaiser & Squires 1993; Miralda-Escudé & Babul 1995).

We have multiple observational ways of cluster mass estimation as mentioned above. However, these methods do not always give us consistent results (Mahdavi et al. 2008). In case of well-known gravitational lensing cluster CL 0024+17, for example, mass derived from X-ray data (Ota et al. 2004) and those from gravitational lensing (Tyson et al. 1998; Broadhurst et al. 2000; Jee et al. 2007) are significantly different, where the latter results are larger than the former by a factor of two or three. Recently, Zhang et al. (2010) made a comparison of X-ray and lensing mass for 12 clusters, and showed that mass of disturbed clusters could be both overestimated and underestimated.

Some assumptions are necessary in the mass estimation method presented above. In the method with line-of-sight galaxy velocities, we assume that the system is in dynamical equilibrium and often assume isotropic velocity distribution of the member galaxies and spherical symmetric structure. In addition, another critical aspect in this method lies in the difficulty of removing foreground and background galaxies, which significantly affect the estimate of the velocity dispersion and mass (Biviano et al. 2006). In the X-ray method we assume that the systems are in hydrostatic equilibrium and spherically symmetric. Simple methods with strong lensing often assume axial symmetry. Even more elaborate methods based on strong lensing technique are essentially model-dependent. Although the weak gravitational lensing method seems to be free from these assumptions about dynamical state and geometry, it does not provides us with three-dimensional mass density distribution but two-dimensional surface-mass density one. This fact should be noted especially when the lensing results are compared with those derived from other methods.

A lot of N -body + hydrodynamical simulations with cosmological initial conditions have been done so far to investigate accuracy of cluster mass estimation (Evrard et al. 1996; Rasia et al. 2006; Kay et al. 2007; Nagai et al. 2007; Piffaretti & Valdarnini 2008; Ventimiglia et al. 2008; Ameglio et al. 2009). It is true that such studies are useful in order to investigate this issue in realistic situations. However, such simulations are not suitable to model a single merger event because it is difficult to control initial conditions and achieve very high resolution in particular interesting regions efficiently. Therefore, studies based on binary merger simulations

are complementary and worthwhile, in which it is relatively easy to keep initial conditions under control, improve numerical resolution, and derive clear physical interpretations. The assumptions for mass estimation listed above are not very good in clusters during or a few Gyr after mergers. Binary merger cluster simulations tell us that mergers generate bulk flow motion and complex temperature structures in the ICM, and anisotropic velocity distribution in DM and galaxies (Roettiger et al. 1996; Takizawa 1999; Takizawa 2000; Ricker & Sarazin 2001; Ritchie & Thomas 2002; Rowley et al. 2004; Ascasibar & Markevitch 2006; Poole et al. 2006; Takizawa 2006; McCarthy et al. 2007; Poole et al. 2007; Springel & Farrar 2007; Akahori & Yoshikawa 2008; Mastropietro & Burkert 2008; ZuHone et al. 2009). Of course, asymmetric spatial structures are also often seen in ICM, DM, and galaxies. However, it is not trivial how these systems will be overestimated or underestimated. This depends on the phase of mergers, geometry of the system and observational direction, and which mass estimation method we use.

In this paper, we adopt the latter approach to investigate the impact of mergers on the cluster mass estimation using N -body+hydrodynamical simulation data. We make mock observational data such as line-of-sight velocity of member galaxies, X-ray brightness distribution, and spectroscopic-like temperature (Mazzotta et al. 2004) maps of ICM from the simulation data. We perform “simulations of mass estimation” for these mock data, and compare the results with actual mass distribution in the simulation data.

The rest of this paper is organized as follows. In §2 we describe the adopted numerical methods and initial conditions for our N -body + hydrodynamical simulations. In §3 we present the results of mass estimation. In §4 we summarize the results and discuss their implications.

2. The Simulations

2.1. Numerical Methods

Numerical methods used here are basically the same as those in Takizawa (2006), whose hydrodynamical part is identical with what was used in Takizawa (2005). In the present study, we consider clusters of galaxies consisting of two components: collisionless particles corresponding to the galaxies and DM, and ideal fluid corresponding to the ICM. When calculating gravity, both components are considered, although the former dominates over the latter. Radiative cooling and heat conduction are not included. We use the Roe total variation diminishing (TVD) scheme to solve the hydrodynamical equations for the ICM (see Hirsch 1990). The Roe scheme is a well-known Godunov-type method with a linearized Riemann solver (Roe 1981). It is relatively simple and good at capturing shocks without any artificial viscosity. Using the MUSCLE approach and a minmod TVD limiter, we obtain second-order accuracy without any numerical oscillations around discontinuities. To avoid negative pressure, we solve the equations for the total energy and entropy conservation simultaneously. This method is often used in astrophysical hydrodynamic simulations where high Mach number flow can occur (Ryu et al. 1993; Wada &

Norman 2001). Gravitational forces are calculated by the Particle-Mesh (PM) method with the standard Fast Fourier Transform technique for the isolated boundary conditions (see Hockney & Eastwood 1988). The size of the simulation box is $(9.40 \text{ Mpc}) \times (4.70 \text{ Mpc})^2$. The number of the grid points is $256 \times (128)^2$. The total number of the N -body particles used in the simulations is also $256 \times (128)^2$, which is approximately 4.2×10^6 .

It is certain that simulations about full history of realistic cluster formation and evolution should include gas cooling, star formation and energy feedback. However, the aim of the paper is to investigate the impact of merger dynamics on the cluster mass estimation in rather idealized conditions in order to clarify physical interpretation. For this reason, we restrict ourselves to consider simulations which do not incorporate radiative cooling, which is dynamically significant only in the cluster core regions.

2.2. Models and Initial Conditions

The equilibrium cluster model used here is essentially the same as what is used in Takizawa (2008) except that there is no magnetic field. Full description is written in section 2 of Takizawa (2008). We consider mergers of two virialized subclusters with an NFW density profile (Navarro et al. 1997) in the Λ CDM universe ($\Omega_0 = 0.25$, $\lambda_0 = 0.75$) for DM. Given the cosmological parameters and halo’s virial mass, we calculate the parameters in the NFW profile following a method in Appendix of Navarro, Frenk, White (1997). The initial density profiles of the ICM are assumed to be those of a beta-model. We assume that the core radius is half of the scale radius of the DM distribution, and that $\beta = 0.6$. The gas mass fraction is set to be 0.1 inside the virial radius of each subcluster. The velocity distribution of the DM particles is assumed to be an isotropic Maxwellian. The radial profiles of the DM velocity dispersion are calculated from the Jeans equation with spherical symmetry, so that the DM particles would be in virial equilibrium in the cluster potential of the DM and ICM. The radial profiles of the ICM pressure are determined in a similar way so that the ICM would be in hydrostatic equilibrium within the cluster potential with a plausible boundary condition. Because the gas density profiles are already given, temperature profiles are automatically determined with an equation of state of the ideal gas. Strictly speaking, the above-mentioned model is in dynamically equilibrium when the spatial distribution of DM and ICM extend to the infinity. In addition, finite spatial resolution of the code could affect the structure and evolution especially in the central region. These issues are discussed in Appendix.

Given each subcluster’s mass and an angular momentum parameter of the system, we estimate “typical” initial conditions for cluster mergers in the same way of Takizawa (2008). We restrict ourselves to analyze head-on mergers because their simple geometrical structures are suitable for the purpose of this paper to clarify physical interpretation of the phenomena. We believe that this choice is fairly reasonable considering that the distribution of impact parameters might be biased to lower values if most mergers occur along large scale structure filament.

Table 1. Model Parameters

	$M_1/M_2(10^{14}M_\odot)$	$r_{\text{vir},1}/r_{\text{vir},2}$ (Mpc)	c_1/c_2	N_1/N_2	$v_{\text{rel.ini}}$ (km s ⁻¹)
Run1:1	5.0/5.0	1.57/1.57	6.12/6.12	2097152/2097152	1360
Run2:1	5.0/2.5	1.57/1.24	6.12/6.60	2796202/1398102	1249
Run4:1	5.0/1.25	1.57/0.987	6.12/7.08	3355443/838861	1210
Run8:1	5.0/0.625	1.57/0.784	6.12/7.56	3728270/466034	1213
Run16:1	5.0/0.3125	1.57/0.622	6.12/8.04	3947580/246724	1239

Off-center merger cases are certainly interesting and important especially to explore more general situations and/or investigate particular observational results, which will be investigated as a future work. How to estimate these conditions is described in detail in Appendix of Takizawa (2008), where the initial relative velocity and impact parameter are calculated through energy and angular momentum conservation laws and some well-known scaling relations predicted from a spherical collapse model (see Peebles 1980). Simulations start in condition that the both subclusters touch each other. Typically, relative initial velocity becomes about two thirds of the infall velocity assuming that they were at rest at infinite distance. This value is similar to the circular velocity of the larger halo at the virial radius. Thus, our initial conditions are quite equivalent to those of controlled merger simulations in Poole et al. (2006) and McCarthy et al. (2007) that are constructed so as to reproduce the merger events found in cosmological simulations. The coordinate system is taken in such a way that the center of mass is at rest at the origin. Two subclusters are initialized in the xy -plane. The collision axis is along the x -axis. The centers of the larger and smaller subclusters were initially located at the sides of $x < 0$ and $x > 0$, respectively.

We analyze the simulation data of head-on collisions whose mass ratios are 1:1, 2:1, 4:1, 8:1, and 16:1. In general, qualitative features are roughly common to all models. Thus, we choose 4:1 merger run as a representative example, whose results will be investigated and described the most intensively. The parameters for each model are summarized in table 1, where M_i , $r_{\text{vir},i}$, c_i , N_i , $v_{\text{rel.ini}}$ are the total mass, virial radius, concentration parameter, number of N -body particles for the i -th subcluster, and initial relative velocity, respectively.

3. Results

3.1. Mass Estimation through Virial Theorem

We “observe” the cluster in the simulation data from a certain direction. Although we can use more than a million particles’ velocity data, it is unrealistic at present to observe such a huge number of member galaxy’s line-of-sight velocities for a single cluster. Thus, we randomly choose N_{samp} particles from the N -body ones within a circle on the sky plain whose center and radius are mass center on the sky plain and a virial radius of the larger cluster listed in table

1, respectively, and recognize them as galaxies whose line-of-sight velocity is observed. Virial mass is calculated following the equation,

$$M_{\text{VT}} = \frac{3\pi}{G} \sigma_{\text{los}}^2 \left\langle \frac{1}{R} \right\rangle^{-1}, \quad (1)$$

where σ_{los}^2 and G are the dispersion of line-of-sight velocities and gravitational constant, respectively. $\langle 1/R \rangle^{-1}$ is the harmonic mean of the distance projected on the sky plain for particle pairs and defined as,

$$\left\langle \frac{1}{R} \right\rangle^{-1} \equiv N_{\text{pair}} \sum_{i>j}^{N_{\text{pair}}} \frac{1}{R_{ij}}, \quad (2)$$

where R_{ij} is the distance projected on the sky plain between i and j -th “observed” galaxies. $N_{\text{pair}} = N_{\text{samp}}(N_{\text{samp}} - 1)/2$ is the number of pairs of “observed” galaxies. Please note that both spherical symmetry and isotropic velocity dispersion are explicitly assumed in this method (see Binney & Tremaine 1987). We estimate virial mass using different N_{tr} sets of “member galaxies” for a single combination of a particular simulation data snapshot and observed direction, and then calculate mean and variance of the virial mass.

In actual observations to determine cluster mass, it is typical that ~ 100 member galaxy’s line-of-sight velocities are available. Even only a few tens of galaxies are sometimes used. Therefore, even if the distributions of galaxies and DM are the same in the phase space, the spatial extent and velocity dispersion of the galaxies sampled sparsely can be significantly different from those of DM. To investigate this, we estimate virial mass for a single relaxed cluster, which is identical to those in the initial conditions of merger simulations, with $N_{\text{tr}} = 100$ and various N_{samp} . Figure 1 shows the dependence of the virial mass 1σ errors upon N_{samp} . Clearly, the errors are proportional to the $1/\sqrt{N_{\text{samp}}}$. The relation is approximately $\Delta \sim 0.2N_{\text{samp}}^{-1/2}$, which means that a few ten percents errors are expected in usual cases ($N_{\text{samp}} \simeq 100$). It should be noted that another systematic errors could occur when galaxies and DM obeys significantly different distribution.

We estimate virial mass in a similar way for merger simulation data with $N_{\text{tr}} = 100$ and $N_{\text{samp}} = 100$, and compare the results to the real mass. However, it is not so trivial what is “real mass” that should be compared with because the system can be non-spherical. Considering that spherical symmetry is assumed in the estimation, mass within a sphere whose center corresponds to the mass center may be valid in theoretical point of view. Figure 2 presents evolution of the ratio of virial mass to “real mass” within the sphere for 4:1 merger. Circles with solid lines and triangles with dashed lines represent results observed from the direction parallel and perpendicular to the collision axis, respectively. Error bars represent 1σ errors in N_{tr} trials of the estimation. Snapshots of mass distribution for this model seen from the direction perpendicular to the collision axis at representative epochs are presented in figure 3.

Here, we describe the comparison of virial mass with real mass within the sphere. When the system is observed along the collision axis, mass tends to be overestimated except during

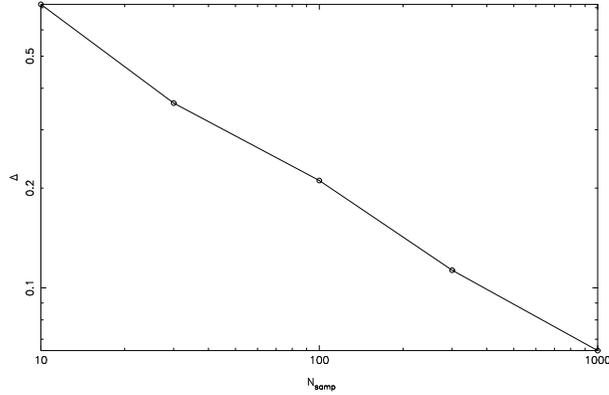


Fig. 1. Dependence of statistical errors of virial mass upon the number of the member galaxy whose line-of-sight velocity can be used in the mass estimation.

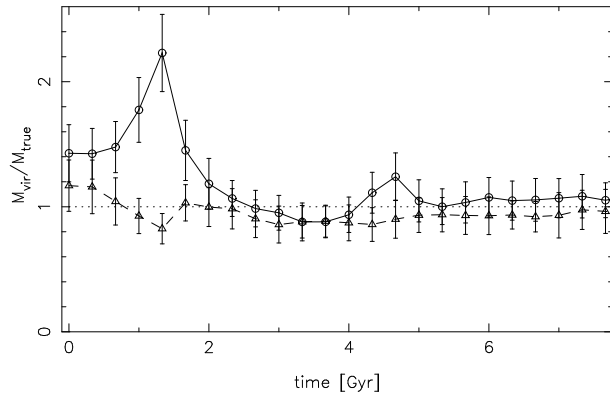


Fig. 2. Evolution of the ratio of virial mass to “real mass” within the sphere for the 4:1 merger. Circles with solid lines and triangles with dashed lines represent results observed from the direction parallel and perpendicular to the collision axis, respectively. Error bars represent 1σ errors in 100 trials of the estimation.

a short period around the apocenter of the subcluster ($t \simeq 3.7\text{Gyr}$). The most serious overestimation is seen at the first core passage ($t \simeq 1.3\text{Gyr}$). The second core passage also cause the second but smaller maximum of overestimation ($t \simeq 4.6\text{Gyr}$). Even after that, mass is systematically overestimated, though this is within the statistical errors. When the system is observed in the direction perpendicular to the collision axis, on the other hand, mass tends to be underestimated except around the initial states. Again, the most serious underestimation occurs at the first core passage. However, the extent of systematic underestimation after that is weak, which is within the statistical errors. It is interesting that the weak dependence of virial mass on the observed direction still remains $\sim 6\text{ Gyr}$ after the core passage.

As we wrote above, the largest systematic errors of virial mass estimation are seen at the first core passage when the system is observed along the collision axis. Naturally, it is expected that this depends on the mass ratio of the smaller subcluster to the larger one. Figure

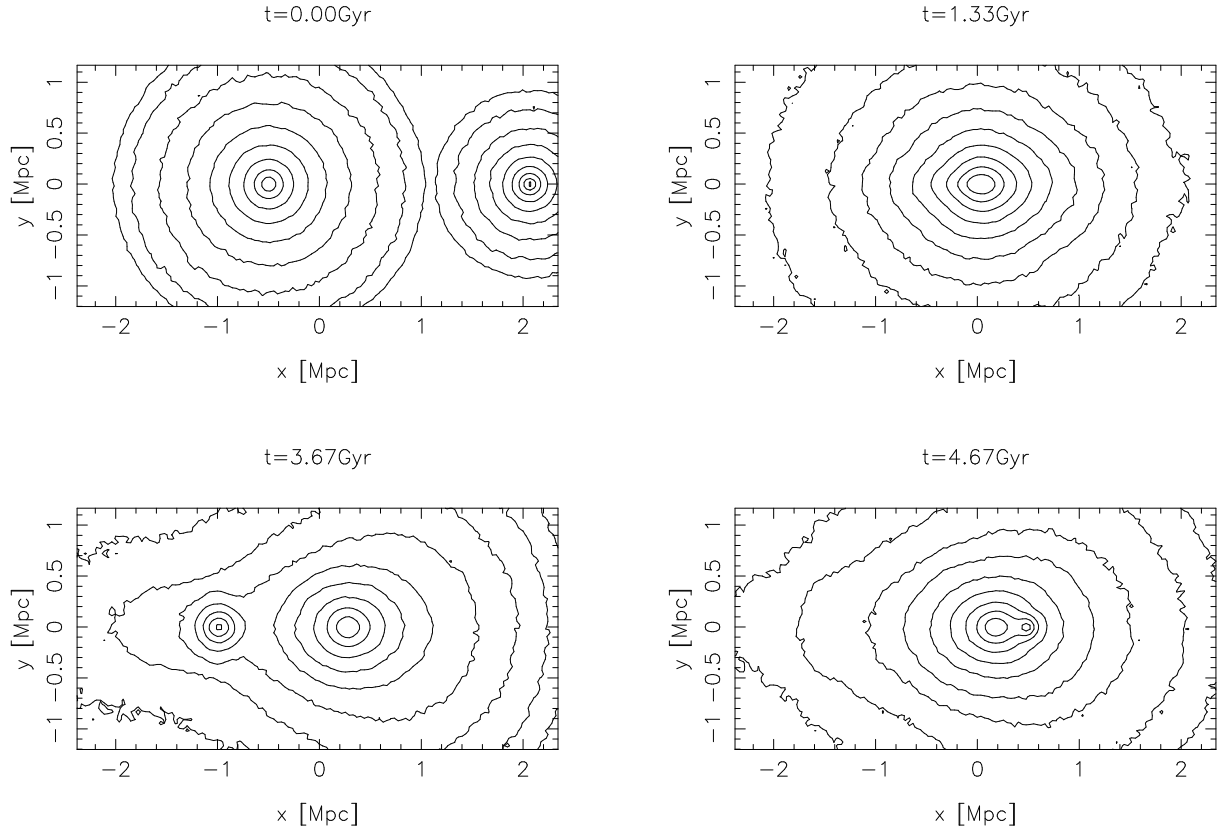


Fig. 3. Snapshots of projected mass distribution for the 4:1 merger model seen from the direction perpendicular to the collision axis.

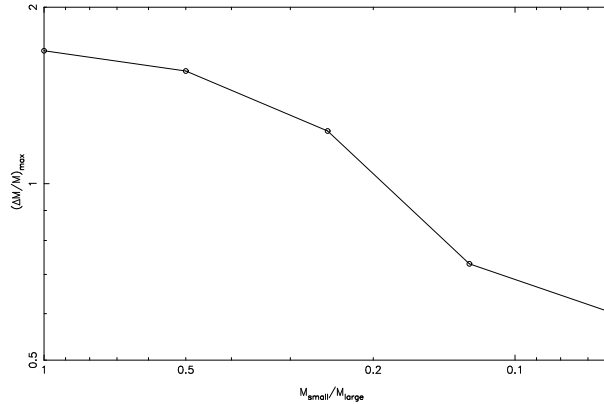


Fig. 4. Dependence of maximum systematic errors of virial mass upon the mass ratio when observed along the collision axis.

4 shows the dependence of the maximum systematic errors of virial mass upon the mass ratio when observed along the collision axis. Roughly speaking, the mass of the system can be overestimated by a factor of more than two when the smaller subcluster’s mass is larger than a quarter of the larger one.

3.2. Mass Estimation with X-ray Data

Again, it is assumed that we “observe” the cluster in the simulation data from a certain direction. We make two-dimensional X-ray brightness distribution and spectroscopic-like temperature (Mazzotta et al. 2004) maps on the sky plain from the three-dimensional simulation data. We determine the image centers from the X-ray brightness maps, and make one-dimensional profiles of the X-ray surface brightness $I_X(R)$ and spectroscopic-like temperature $T_{\text{sl}}(R)$, where R is the distance projected on the sky plain from the image center. The radial density profiles $\rho_g(r)$, where r is the radial distance, are calculated in a standard deprojection procedure assuming spherical symmetry. This deprojection procedure is not done for temperature and we use T_{sl} for mass estimation. Both $\rho_g(r)$ and $T_{\text{sl}}(r)$ are fitted by the β -model function. If a single β -model function fit is not acceptable, we use a so-cold double β -model, which is represented by a sum of two independent β model functions. Assuming hydrostatic equilibrium, the mass profile derived from the X-ray observation is,

$$M_X(r) = -\frac{k_B T_{\text{sl}} r}{G \mu m_p} \left(\frac{d \ln \rho_g}{d \ln r} + \frac{d \ln T_{\text{sl}}}{d \ln r} \right), \quad (3)$$

where k_B , μ , and m_p are the Boltzmann constant, mean molecular weight, and proton mass, respectively. It should be noted that the double β -model function shows rather small gradient around an intersection of each β -model function. This possibly causes unphysical structures in the estimated mass profile through equation (3).

Figure 5 and 6 present snapshots of the X-ray surface brightness distribution (contours) overlaid with spectroscopic-like temperature one (colors) of the 4:1 merger for the representative epochs same as in figure 3 observed in the direction perpendicular and parallel to the collision axis, respectively. The bow shock is just in the center at $t = 1.33$ Gyr. Kelvin-Helmholtz instability develops and non axially symmetric structures are clearly seen at $t = 3.67$ Gyr when observed along the collision axis.

First, we compare the estimated mass profiles derived from equation (3) with those of the actual mass. When calculating an actual mass profile, its center is set at that of the X-ray emissivity except for the data at $t = 0.0$ Gyr. In that case, this definition of the center is not good because the emissivity center is located in relatively low density region between two subclusters. Therefore, we simply set the mass profile center at that of the larger subcluster. Figure 7 shows the radial profiles of the actual mass (solid lines) and estimated mass (dashed lines) for the data presented in figure 5 (lower panels) and 6 (upper panels). Virial mass is also presented in asterisks, although it should be noted that the ways to determine the centers are not common in both the mass estimation methods. Figure 8 shows the same as figure 7, but for the radial profiles of the ratio of the estimated mass to the real mass. Again, the ratio of Virial mass is also represented in asterisks. When the system is observed along the collision axis at $t = 0.00$ Gyr, mass is systematically underestimated at all radii. This is because the projected temperature becomes lower owing to the cooler gas of the smaller subcluster. This results is

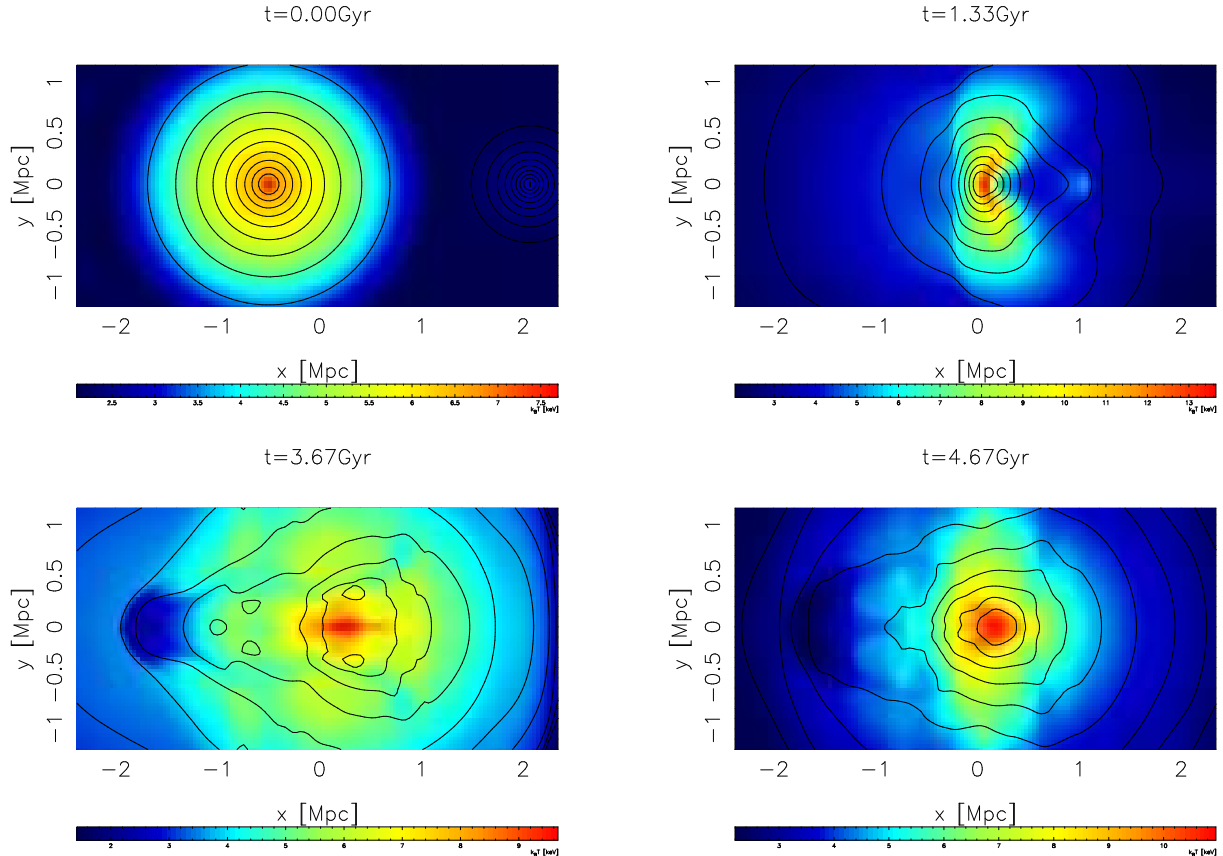


Fig. 5. Snapshots of X-ray surface brightness distribution (contours) and spectroscopic-like temperature map (colors) for the 4:1 merger model seen from the direction perpendicular to the collision axis.

inconsistent with the virial mass estimation. In case of observation along the collision axis at $t = 1.33$ Gyr, while virial mass estimation results in vast overestimation, X-ray mass estimation results in fairly good agreement with the actual mass although the slight underestimation is seen in the outer region. Similar trends are seen when observed in the direction perpendicular to the collision axis at that time, while the both methods lead consistent results. At $t = 3.67$ Gyr, the ratio of the X-ray mass to the real mass shows complex and stronger radial dependence when observed along the collision axis, while the estimation in the direction perpendicular to the axis results in simple underestimation. Negative gradients in the estimated mass profile, which are not physically reasonable, are seen in the panels of “ $t = 3.67$ Gyr, parallel” and “ $t = 4.67$ Gyr, vertical” of figure 7. We checked the X-ray image fitting results and confirmed that these systems were fitted by the double β -model and that these structures occurs around the intersection of each β -model function. Thus, we conclude that these strange structures in the mass profiles are because of artifacts of double β -model fit.

It is worthwhile to compare projected mass profiles calculated from estimated radial mass profiles with real projected mass profiles, which is directly obtained from gravitational lensing analysis. The projected mass profile is,

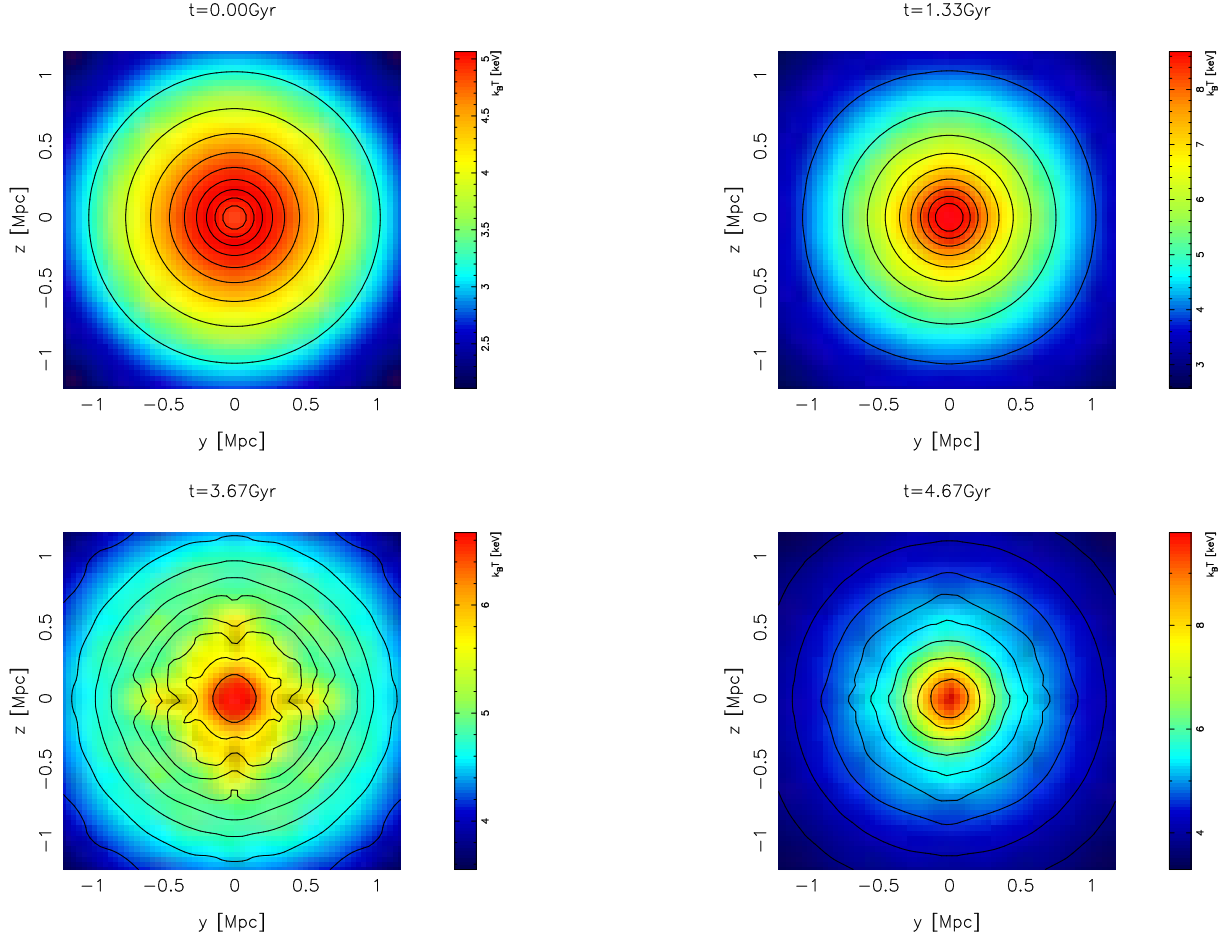


Fig. 6. Same as figure 5, but seen from the direction parallel to the collision axis.

$$M_{\text{prj}}(R) = \int_0^R 2\pi R' \Sigma(R') dR', \quad (4)$$

$$\Sigma(R) = 2 \int_0^{b_{\text{out}}} \rho(\sqrt{R^2 + b^2}) db, \quad (5)$$

where Σ is the surface mass density. The mass density $\rho(r)$ is calculated from the radial mass profile as follows,

$$\rho(r) = \frac{1}{4\pi r^2} \frac{dM}{dr}. \quad (6)$$

Figure 9 presents the same as figure 7, but for the projected mass profiles of real mass (solid lines) and estimated mass (dashed lines). Virial mass is also represented in asterisks. Again, it should be noted that the centers can be different in both methods for the same data. Figure 10 also shows the same as figure 8, but for the projected mass. The merging system tends to be elongated towards the collision axis in three-dimensional mass distribution. As a result, the estimated project mass under the assumption of spherical symmetry tends to be smaller and larger when observed from the direction parallel and perpendicular to the collision axis, which cause underestimation and overestimation trends, respectively. The unphysical structures in

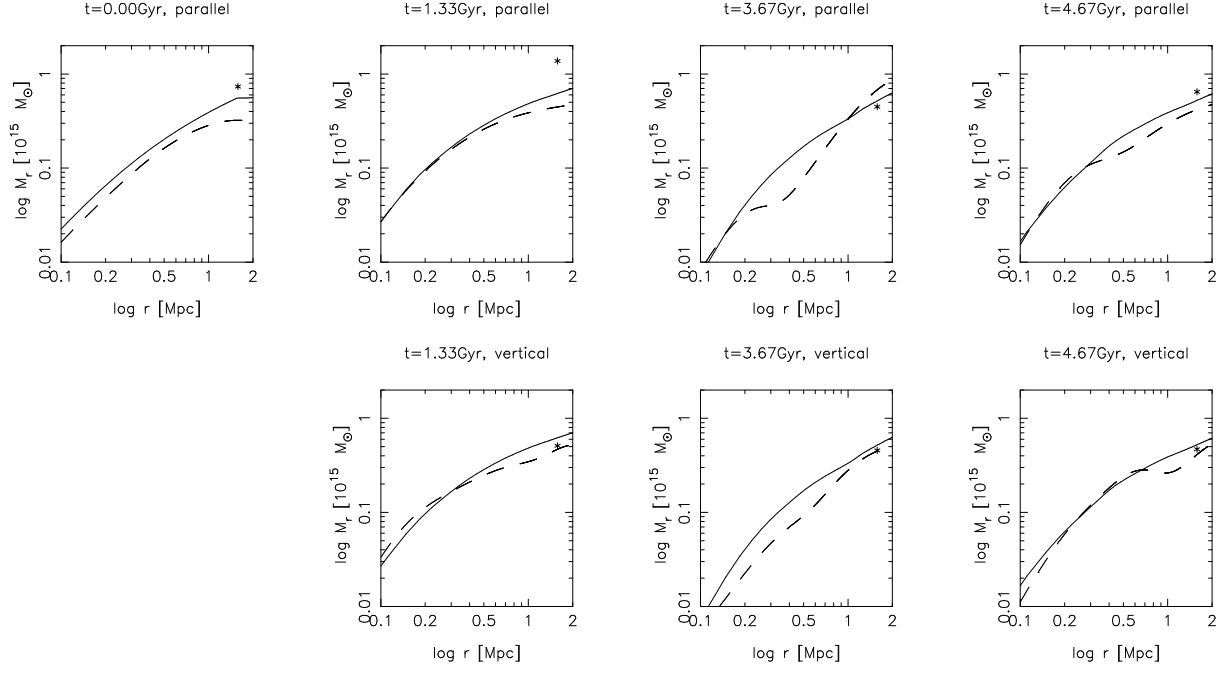


Fig. 7. Radial profiles of actual mass (solid lines) and estimated mass from X-ray data (dashed lines) for the 4:1 merger. Virial mass is also represented in asterisks. Upper and lower panels show the mass profiles seen from the direction parallel and perpendicular to the collision axis, respectively.

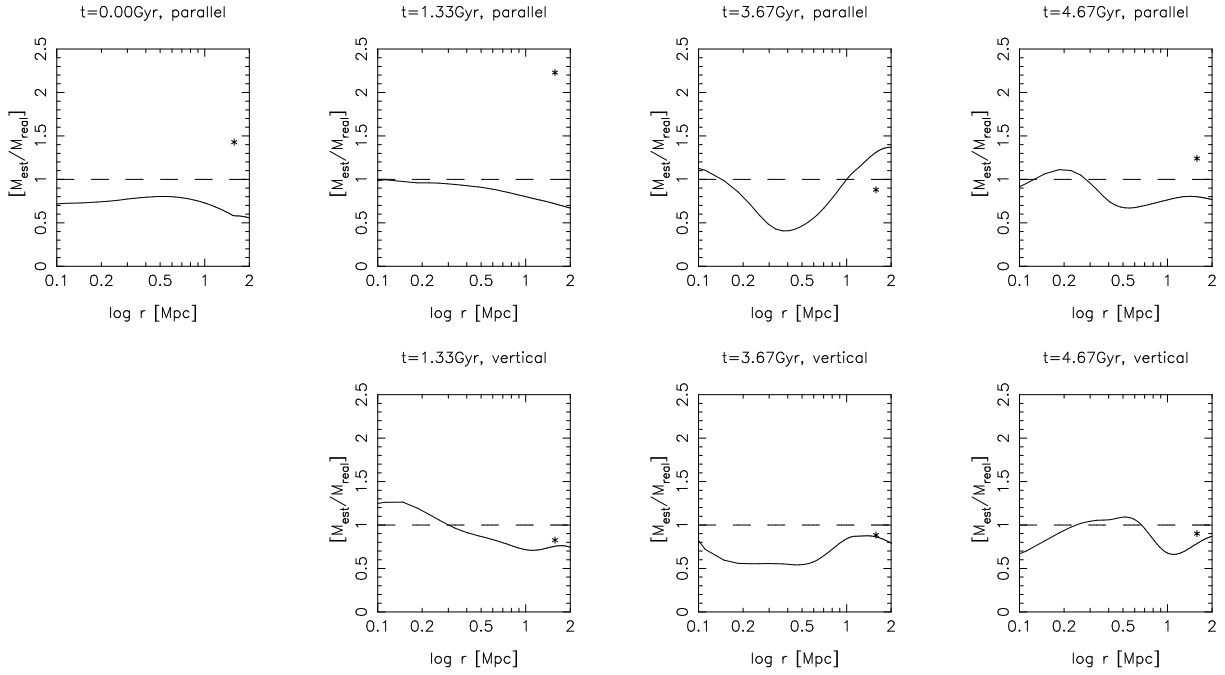


Fig. 8. Same as figure 7, but for the radial profiles of the ratio of estimated mass with X-ray data to the real mass (solid lines). The results with Virial mass are also represented in asterisks.

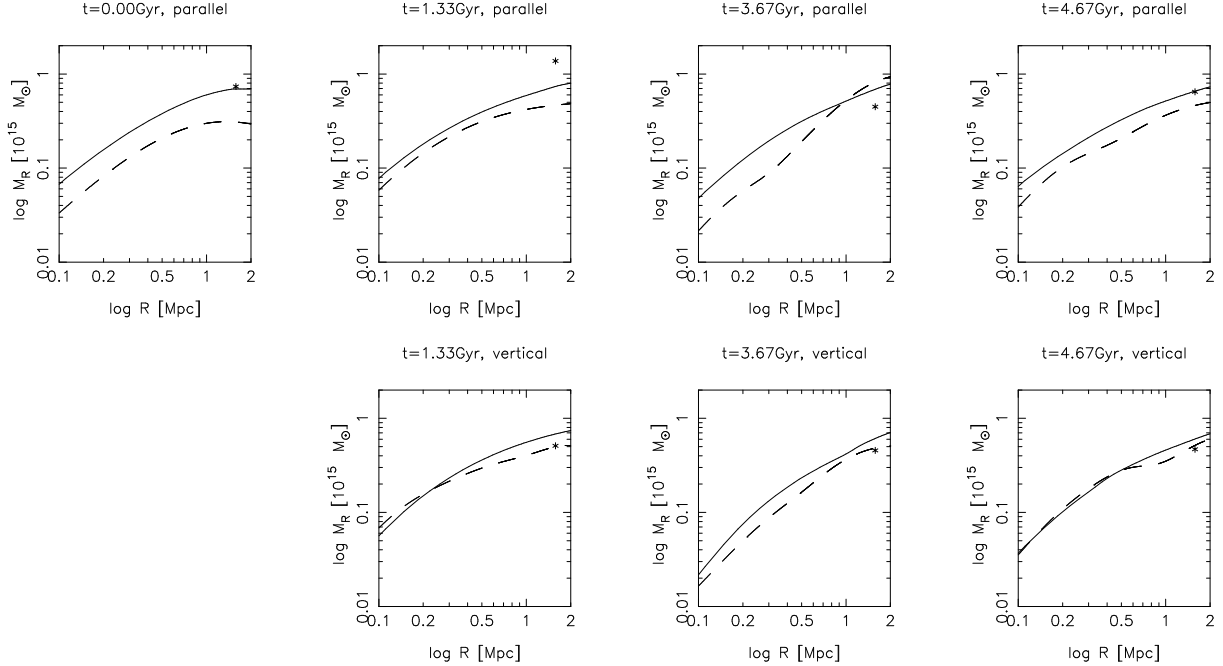


Fig. 9. Same as figure 7, but for the projected mass profiles of actual mass (solid lines) and estimated mass from the X-ray data (dashed lines). Again, Virial mass is also represented in asterisks.

mass profiles because of the artifacts of double β model fit are also slightly recognized in figure 9 though they are much less prominent than in spherical mass profiles.

3.3. Density and Temperature Profile Models

The mass estimation results can depend on the modeling of density and temperature profiles (Piffaretti & Valdarnini 2008). In fact, some of our results show unphysical structures in the mass profile caused by the artifact of double beta model fit. In order to check this fact we estimate the mass from the X-ray data using the density and temperature profile models, which are believed to be more sophisticated, proposed by Vikhlinin et al. (2006) as follows,

$$n_e n_p = n_0^2 \frac{(r/r_c)^{-\alpha}}{(1 + r^2/r_c^2)^{3\beta - \alpha/2}} \frac{1}{(1 + r\gamma/r_s^\gamma)^{\epsilon/\gamma}} + \frac{n_{02}^2}{(1 + r^2/r_{c2}^2)^{3\beta_2}}, \quad (7)$$

$$T(r) = T_0 \frac{(r/r_t)^{-a}}{\left[1 + (r/r_t)^b\right]^{c/b}}, \quad (8)$$

where we do not use the functional part for the central cool core component in the original form because clusters used here correspond to so-called non cooling core clusters. Using these models instead of the β -model, we estimate a radial mass profile for the X-ray data of the standard run in a similar way in subsection 3.2. Figure 11 shows the same as figure 7, but for the density and temperature models of equation (7) and (8). In general, the results are quite similar. A negative gradient in the mass profile is still seen even with these models.

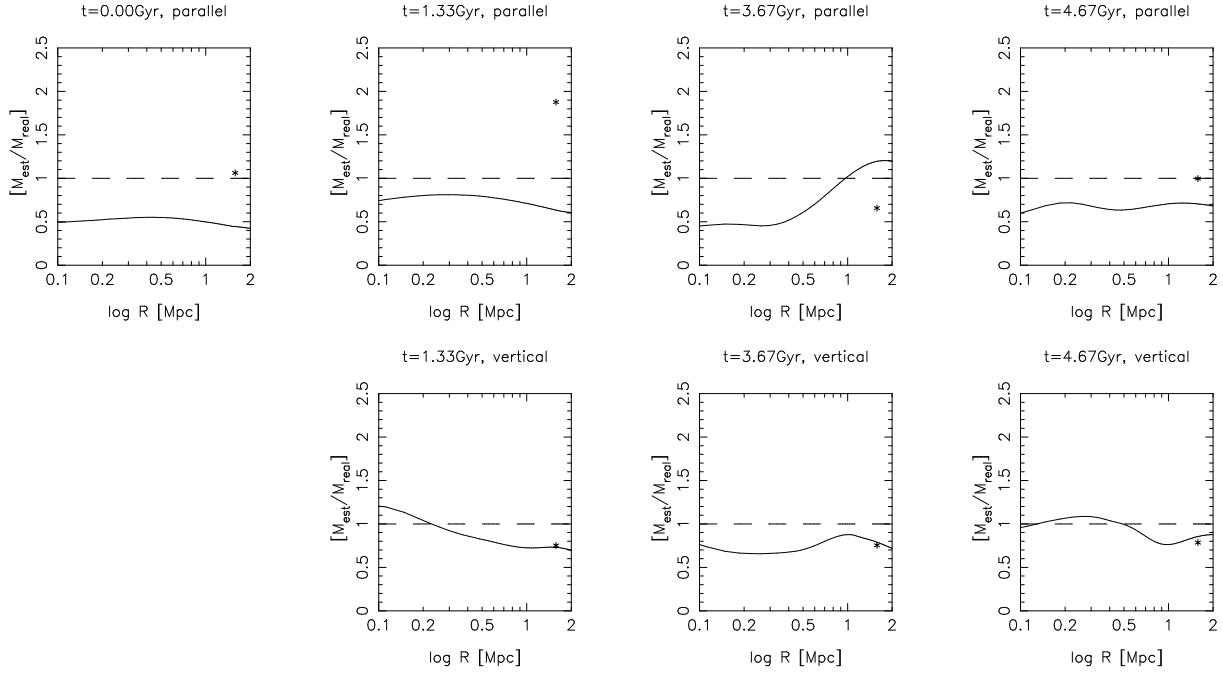


Fig. 10. Same as figure 8, but for the projected mass. The results with virial mass are also represented in asterisks.

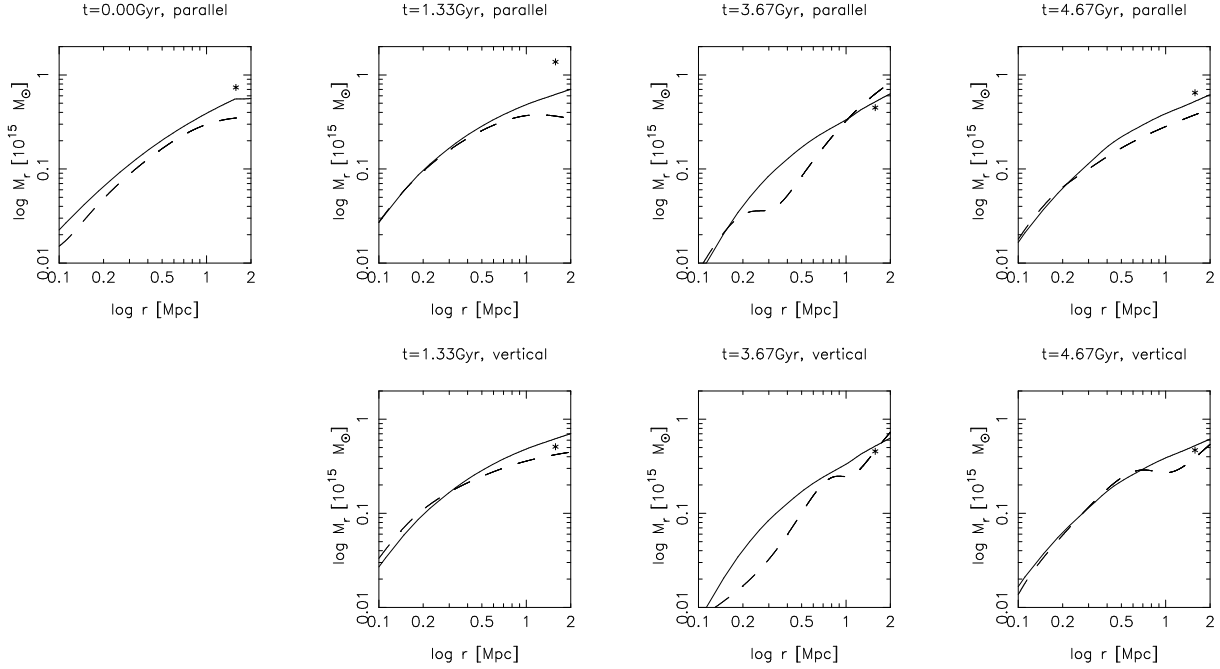


Fig. 11. Same as figure 7, but for using density and temperature profile models proposed by Vikhlinin et al. (2006) instead of β -model.

4. Summary and Discussion

We investigate the impact of mergers on the mass estimation of galaxy clusters using N -body + hydrodynamical simulation data. We randomly select a part of N -body particles and recognize them as galaxies whose line-of-sight velocity is observed. We estimate virial mass from these data and compare it with actual mass. The results strongly depend on the observational directions mainly because of anisotropic velocity distribution. When observed along the collision axis, the mass of the system tends to be overestimated. When the smaller cluster mass is larger than a quarter of the larger one, the virial mass can be larger than twice of the real mass. We also make the X-ray surface brightness and spectroscopic-like temperature maps from the simulation data. Mass profiles are calculated from these “X-ray observational data” under the assumption of hydrostatic equilibrium. Again, the estimated mass profiles are compared with those of actual mass. In general, mass estimation with X-ray data gives us fairly better results than Virial mass estimation. The dependence upon the observational directions is weaker, because the gas pressure is isotropic, and because anisotropic temperature fluctuations are smoothed out in azimuthal direction. When the systems are observed along the collision axis, the projected mass tends to be underestimated. This fact should be noted when the Virial and/or X-ray mass are compared with gravitational lensing results.

4.1. Mass Estimation Uncertainty and the Morphology of X-ray Image

It is useful to discuss the relationship between the mass estimation uncertainty and the morphology of X-ray image. One may easily guess that clusters with an extremely elongated X-ray image (e.g., the snapshot at $t=3.67$ Gyr in figure 5) are not in hydrostatic equilibrium. Indeed, the mass is systematically underestimated in this system (see “ $t=3.67$ Gyr, vertical” panel in Fig8). Roughly speaking, the X-ray mass estimation results in underestimation of 20-40 %. In other word, mass can be estimated as accurately as within a factor of two even for such an irregular cluster. The estimation accuracy becomes better for the projected mass comparison (e.g., the snapshot at $t=3.67$ Gyr in figure 10). This is because the underestimation trend caused by irregular morphology and bulk flow motion is partly compensated by the overestimation trend caused by the projection effect.

To quantify the image morphology, we use the axial ratio of the surface brightness image defined through the second moments of the surface brightness,

$$M_{ij} = \sum I_X x_i x_j, \quad (9)$$

where the summation is conducted over the coordinates whose origin is at the X-ray peak and within a certain aperture centered on the origin (O’hara et al. 2006). Our models have axial symmetry for the collision axis (x -axis). Therefore, we only need to calculate M_{11} and M_{22} and do not have to diagonalize the matrix M for the X-ray images seen from the direction perpendicular to the collision axis, when we choose the x_1 and x_2 axes to be parallel to the x

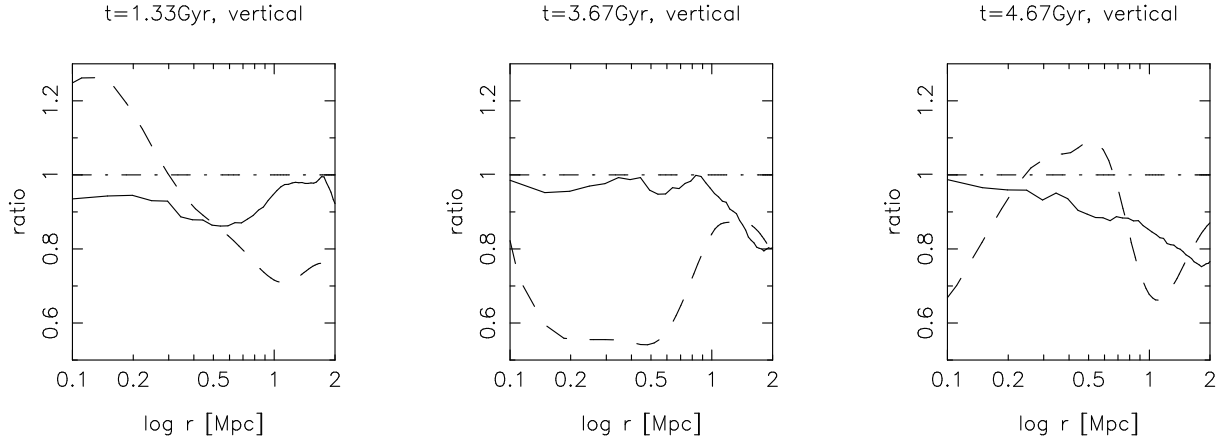


Fig. 12. The axial ratio of the X-ray surface brightness as a function of the aperture radius (solid line) and ratio of estimated mass with X-ray data to the real mass (dashed lines) for the standard run seen from the direction perpendicular to the collision axis.

and y , respectively. We actually calculate $M_{12}(=M_{21})$ and confirm that $|M_{12}/M_{ii}|$ is typically ~ 0.005 . Then, the axial ratio η is defined as,

$$\eta = \begin{cases} M_{11}/M_{22}, & M_{11} \leq M_{22}, \\ M_{22}/M_{11}, & M_{11} > M_{22}. \end{cases} \quad (10)$$

Thus, the axial ratio lies between 0 and 1 by definition, and $\eta = 1$ means a circular cluster. In some clusters with complex morphology, such as ones with three or more peaks, the axial ratio is not a good indicator (Ventimiglia et al. 2008). However, because our model clusters tends to have a relatively simple elliptical shape, it does not matter. Figure 12 shows the η as a function of the aperture radius (solid lines) and the ratio of estimated and real mass (dashed lines) for the standard run seen from the direction perpendicular to the collision axis. It is interesting that the inner region is nearly circular ($\eta \simeq 1$) but mass estimation error is relatively large at $t = 3.67$ and 4.67 Gyr. This means that the morphology determined from only inner region is not a good indicator of mass estimation error, which should be cared especially for the distant faint clusters.

On the other hand, it should be noted that clusters with spherical and regular X-ray morphology do not always result in good mass estimation. This is especially true for head-on merger clusters observed nearly along the collision axis. Spherical mass can be both overestimated and underestimated, depending on the radial distance and the phase of merger, although the results tend to be more accurate than in case of virial mass (see upper panels in figure 8). About $\sim 20\%$ errors are typically seen. Even nearly 50% errors can be found in the “ $t=3.67$ Gyr, parallel” panel in figure 8. As for the projected mass results, however, the situation is a little bit different, where the X-ray mass is systematically smaller than the real mass (see the upper panels in figure 10). In these cases, $\sim 50\%$ underestimations can occur. In both cases, anyway, it should be noted that X-ray and virial mass estimations give us inconsistent results, and that

both are significantly different than the real mass, although the X-ray image is quite symmetric. This implies that these clusters do not follow the correlation between X-ray temperature and galaxy velocity dispersion for relaxed clusters. In other words, these clusters show a peculiar β_{spec} value, which has been already recognized as a good indicator for merging clusters (Ishizaka 1996; Takizawa 2000). These results can qualitatively explain the discrepancy between X-ray and lensing mass reported in CL 0024+17 (Ota et al. 2004; Jee et al. 2007).

Recently, ZuHone et al. (2009) studied a line-of-sight galaxy cluster collision using numerical simulations, and compared their results with Cl 0024+17 in detail. Their results are basically consistent with ours, but there are several differences. As seen in figure 10, systematic underestimation trends are clearly seen in the projected mass when observed along the collision axis, which is qualitatively consistent with theirs. As written in subsection 2.2 of ZuHone et al. (2009), their collision velocity is approximately twice of the free fall velocity. This is an extremely rare case in the CDM universe though it might be good for reproducing the Cl 0024+17 results. On the other hand, the collision velocities in our simulations are comparable to but a little bit smaller than the free fall one, which means a more usual case. Thus, it is not surprising that ZuHone et al. (2009) shows more serious underestimation, and that their results are quantitatively different than ours. In addition, though both ZuHone et al. (2009) and our models used the double-beta model fitting, its interpretation and resultant procedure of mass estimation are different. ZuHone et al. (2009) assumes that double-beta surface brightness distribution means two individual spherical clusters aligned along the line-of-sight. Therefore, they calculate hydrostatic mass for two spherical clusters and sum them in deriving projected mass. On the other hand, we assume that the double-beta surface brightness distribution means a single spherical cluster with a relatively complex density profile that cannot be well represented by a single beta-model (Ikebe et al. 2004). Thus, we calculate hydrostatic mass for a single spherical cluster.

4.2. ICM Internal Velocity

It is quite natural that ICM internal velocity as well as member galaxies' velocities can be another probe of merger dynamics and mass estimation uncertainty. In addition, although subclusters are in hydrostatic equilibrium in the initial conditions in our merger simulations, it is most likely that clusters before major mergers have already undergone some mergers in the CDM universe. As a result, the merger progenitors could have significant bulk and/or turbulent flow motions in the ICM. This causes additional underestimation in mass measurement with X-ray data (Fang et al. 2009). Anyway, firm direct detection of ICM motion is highly desired in this regard though this is not an easy task in the current status of X-ray astronomy (e.g. Ota et al. 2007; Fujita et al. 2008; Sugawara et al. 2009). The ASTRO-H satellite (former NeXT; e.g. Takahashi et al. 2006), which is planned to be launched around 2013, will enable us to measure the line-of-sight velocity directly with the X-ray microcalorimeters and provide

us with useful information on the dynamical status of the ICM. Another possible observational approach to the ICM motion is the Sunyaev-Zel'dovich (SZ) effect. In principle, the line-of-sight and tangential velocity components can be measured with the kinematic SZ effect and SZ polarization, respectively (Sunyaev & Zel'dovich 1980), though they are still challenging in the present status of the observations.

4.3. Member Galaxy Distribution

As mentioned above, we sampled particles corresponding to the member galaxies from N -body particles in virial mass estimation. This means that the phase space distribution of the galaxies are assumed to be essentially the same as that of DM. However, it is likely that this assumption is not so good in realistic situations. Using cosmological simulations that include cooling and star formation, Nagai & Kravtsov (2005) showed that the concentration of the radial distribution of simulated galaxies is lower than that of dark matter even for relaxed systems, thereby implying errors in the mass estimation through the virial theorem. On the other hand, our aim is to evaluate errors caused by dynamical motions during mergers, therefore, for systems that are far from dynamical equilibrium. We conclude that our findings about virial mass estimates are not significantly affected by such biases (Nagai & Kravtsov 2005).

M. T. would like to thank N. Okabe, M. Takada, and M. Nagashima for helpful comments. The authors are grateful to an anonymous referee for his/her useful comments and suggestions which improved the manuscript. Numerical computations were carried out on VPP5000 and XT4 at the Center for Computational Astrophysics, CfCA, of the National Astronomical Observatory of Japan. M. T. was supported in part by a Grant-in-Aid from the Ministry of Education, Science, Sports, and Culture of Japan (16740105, 19740096).

Appendix. Evolution of the Equilibrium Model Cluster

Our initial cluster model is in dynamical equilibrium when the spatial distribution of DM and ICM extend to the infinity. Strictly speaking, this is not the case for the actual simulations. In addition, finite spatial resolution of the code could affect the structure and evolution especially in the central region. To check these issues, we perform the run of a single cluster where the initial conditions are the same as those of the larger cluster in the standard run. Figure 13 shows the radial profiles of various physical values, where the dashed and solid lines represents the profiles at $t = 0$ and 4 Gyr, respectively. The DM density profile in the central region becomes slightly flatter but still has the cuspy structure. In the outer region, DM density profile change is much less significant. The shape of the DM velocity dispersion profiles does not change significantly for both radial and tangential components and the velocity distribution keeps to be isotropic, although the absolute value of the velocity dispersions become slightly smaller. Similar trends are seen in the ICM radial density and temperature profiles.

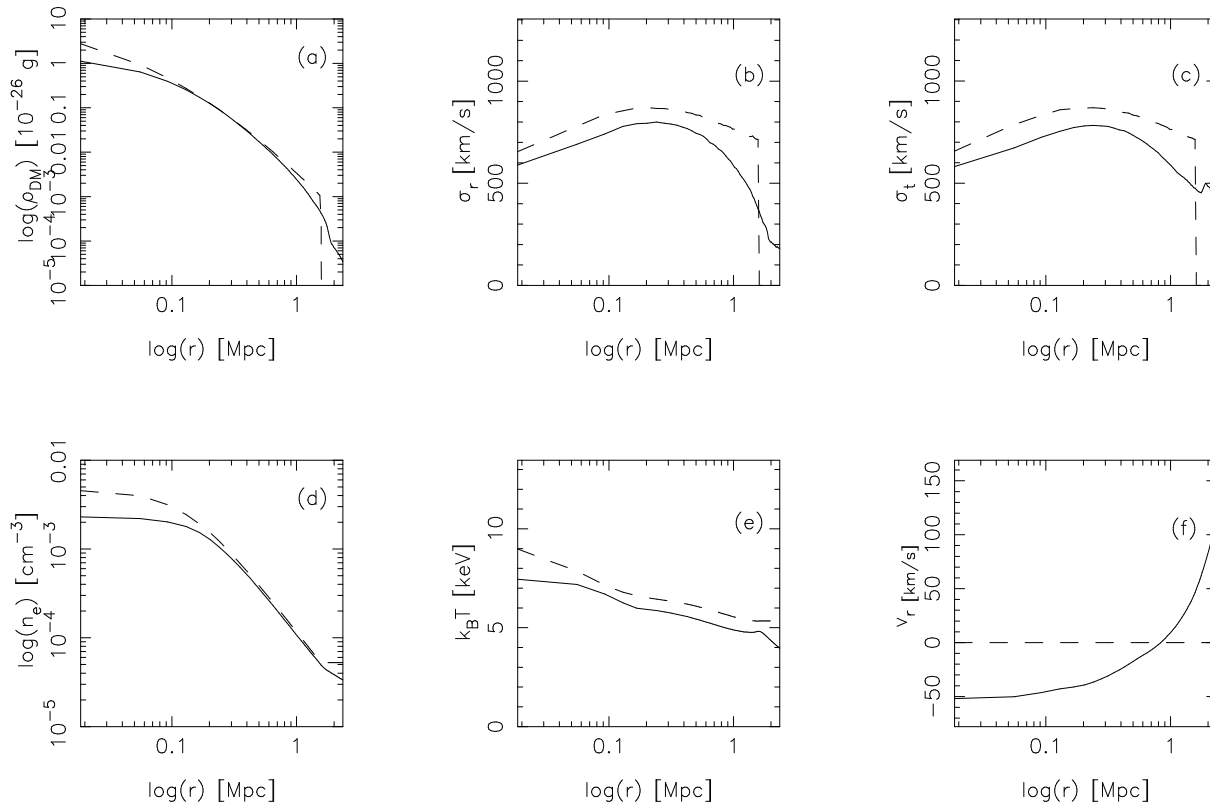


Fig. 13. The radial profiles of (a) DM density, (b) standard deviation of DM radial velocity, (c) that of tangential velocity, (d) electron number density of ICM, (e) ICM temperature, and (f) radial velocity of ICM for the equilibrium cluster model. The dashed and solid lines show the profiles at $t = 0$ and 4 Gyr, respectively.

The ICM has finite radial velocity at $t = 4$ Gyr, which is much less than the sound velocity.

It is certain that our initial model shows some signs of evolution quantitatively. However, its impact for mass estimation is very limited. For example, typical values of the excited radial velocity of the ICM ($\sim 50 \text{ km s}^{-1}$) is much smaller than the sound velocity of 7 keV ICM ($\sim 1400 \text{ km s}^{-1}$), as in shown figure 13. This means that the kinetic energy of the ICM is only $\sim 0.1\%$ of the thermal one. As for the dark mater component, we actually checked the results of Virial mass estimation for the data shown in figure 13, and confirmed that the errors becomes only less than $\sim 10\%$, which is smaller than typical statistical errors with $N_{\text{samp}} = 100$. These effects are clearly smaller than the impact of merger itself. Therefore, we think that our initial model is suitable enough for the main purpose of this paper.

We actually followed the time evolution of the isolated initial model cluster for 5 Gyr. However, we did not see transition to another equilibrium configuration. Even if we possibly find another equilibrium configuration after the much longer run, we do not think that the configuration is much preferable for the initial conditions, considering that it could be significantly altered from the NFW profile that represents the structure of dark halos found in cosmological

simulations reasonably well.

References

- Akahori, T., & Yoshikawa, K. 2008, PASJ, 60, L19
- Ameglio, S., Borgani, S., Pierpaoli, E., Dolag, K., Ettori, S., & Morandi, A. 2009, MNRAS, 394, 479
- Ascasibar, Y., & Markevitch, M. 2006, ApJ, 650, 102
- Barrena, R., Boschini, W., Girardi, M., Spolaor, M. 2007, A&A, 469, 861
- Biviano, A., Murante, G., Borgani, S., Diaferio, A., Dolag, K., Girardi, M. 2006, A&A, 456, 23
- Binney, J., & Tremaine, S. 1987, Galactic Dynamics (Princeton: Princeton Univ. Press)
- Bradač, M. et al. 2006, ApJ, 652, 937
- Broadhurst, T., Huang, X., Frye, B., & Ellis, R. 2000, ApJL, 534, L15
- Clowe, D., Gonzalez, A., Markevitch, M. 2004, ApJ, 594, 604
- Evrard, A. E., Metzler, C. A., & Navarro, J. F. 1996, ApJ, 469, 494
- Fang, T., Humphrey, P. & Buote, D. 2009, ApJ, 691, 1648
- Fujita, Y. et al. 2008, PASJ, 60, 1133
- Gastaldello, F., Buote, D. A., Humphrey, P. J., Zappacosta, L., Bullock, J. S., Brighenti, F., Mathews, W. G. 2007, ApJ, 669, 158
- Girardi, M., Giuricin, G., Mardirossian, F., Mezzetti, M., & Boschini, W. 1998, ApJ, 505, 74
- Hirsch, C. 1990, Numerical Computation of Internal and External Flows (New York: John Wiley & Sons)
- Hockney, R. W., & Eastwood, J. W. 1988, Computer Simulation Using Particles (London: Institute of Physics Publishing)
- Ikebe, Y., Böhringer, H., & Kitayama, T. 2004, ApJ, 611, 175
- Ishizaka, C. 1997, Ap&SS, 254, 233
- Jee, M. J. et al. 2007, ApJ, 661, 728
- Jelteman, T. E., Hallman, E. J., Burns, J. O., & Molt, P. M. 2008, ApJ, 681, 167
- Kay, S. T., de Silva, A. C., Aghanim, N., Blanchard, A., Liddle, A. R., Puget, J., Sadat, R., & Thomas, P. A. 2007, MNRAS, 377, 317
- Kent, S. M., & Gunn, J. E. 1982, AJ, 87, 945
- Kaiser, N., & Squires, G. 1993, ApJ, 404, 441
- Mahdavi, A., Hoekstra, H., Babul, A., & Henry, J. P. 2008, MNRAS, 384, 1567
- Mastropietro, C., & Burkert, A. 2008, MNRAS, 389, 967
- Maurogordato, S. et al. 2008, A&A, 481, 593
- Mazzotta, P., Rasia, E., Moscardini, L., & Tormen, G. 2004, MNRAS, 354, 10
- McCarthy, I. G. et al. 2007, MNRAS, 376, 497
- Miralda-Escudé, J. & Babul, A. 1995, ApJ, 449, 18
- Nagai, D., & Kravtsov, A. V. 2005, ApJ, 618, 557
- Nagai, D., Vikhlinin, A., & Kravtsov, A. V. 2007, ApJ, 655, 98
- Navarro, J. F., Frenk, C. S., & White, S. D. M. 1997, ApJ, 490, 493
- Oegerle, W. R., & Hill, J. M. 1994, AJ, 107, 857

O'Hara, T. B., Mohr, J. J., Bialek, J. J., Evrard, A. E. 2006, *ApJ*, 639, 640

Okabe, N., & Umetsu, K. 2008, *PASJ*, 60, 345

Ota, N, Pointecouteau, E., Hattori, M., & Mitsuda, K. 2004, *ApJ*, 601, 120

Ota, N. et al. 2007, *PASJ*, 59, 351

Peebles, P. J. E. 1980, *The Large-Scale Structure of the Universe* (Princeton: Princeton Univ. Press)

Piffaretti, R., & Valdarnini, R. 2008, *A&A*, 491, 71

Poole, G. B., Fardal, M. A., Babul, A., McCarthy, I. G., Quinn, T., Wadsley, J. 2006, *MNRAS*, 373, 881

Poole, G. B., Babul, A., McCarthy, I. G., Fardal, M. A., Bildfell, C. J., Quinn, T., Mahdavi, A. 2007, *MNRAS*, 380, 437

Reiprich, T. H., & Böhringer, H. 2002, *ApJ*, 567, 716

Rasia, E. et al. 2006, *MNRAS*, 369, 2013

Ricker, P. M., & Sarazin, C. L. 2001, *ApJ*, 561, 624

Ritchie, B. W., & Thomas, P. A. 2002, *MNRAS*, 329, 675

Roe, P. L. 1981, *J. Comput. Phys.*, 43, 357

Roettiger, K., Burns, J. O., & Loken, C. 1996, *ApJ*, 473, 651

Rowley, D. R., Thomas, P. A., & Kay, S. T. 2004, *MNRAS*, 352, 508

Ryu, D., Ostriker, J. P., Kang, H., & Cen, R. 1993, *ApJ*, 414, 1

Springel, V., & Farrar, G. R. 2007, *MNRAS*, 380, 911

Sugawara, C., Takizawa, M., & Nakazawa, K. 2009, *PASJ*, 61, 1293

Sunyaev, R. A., & Zel'dovich, Ya. B. 1980, *MNRAS*, 190, 413

Takahashi, T., Mitsuda, K., & Kunieda, H. 2006, *SPIE proc.*, 6266

Takizawa, M. 1999, *ApJ*, 520, 514

Takizawa, M. 2000, *ApJ*, 532, 183

Takizawa, M. 2005, *ApJ*, 629, 791

Takizawa, M. 2006, *PASJ*, 58, 925

Takizawa, M. 2008, *ApJ*, 687, 951

Takizawa, M., Sarazin, C. L., Blanton, E. L., Taylor, G. B. 2003, *ApJ*, 595, 142

Tyson, J. A., Kochanski, G. P., & Dell'antonio, I. P. 1998, *ApJ*, 498, L107

Ventimiglia, D. A., Voit, G. M., Donahue, M., & Ameglio, S. 2008, *ApJ*, 685, 118

Vikhlinin, A., Kravtsov, A., Forman, W., Jones, C., Markevitch, M., Murray, S. S., Van Speybroeck, L. *ApJ*, 640, 691

Wada, K., & Norman, C., A. 2001, *ApJ*, 547, 172

Yoshida, N., Springel, V., White, S. D. M., & Tormen, G. 2000, *ApJ*, 544

Zhang, Y. et al. 2010, *ApJ*, 711, 1033

ZuHone, J. A., Ricker, P. M., Lamb, D. Q., & Karen Yang, H.-Y., 2009, *ApJ*, 699, 1004